MOLECULAR IMAGING AND BIOLOGY

Published Online: 23 July 2011

Mol Imaging Biol (2012) 14:286–292
DOI: 10.1007/s11307-011-0510-6

RESEARCH ARTICLE

Fast-Specific Tomography Imaging *via* Cerenkov Emission

Jianghong Zhong, Chenghu Qin, Xin Yang, Zhe Chen, Xiang Yang, Jie Tian

Intelligent Medical Research Center, Institute of Automation, Chinese Academy of Sciences, Room 931, Automation Building, No.95 Zhongguancun East Road, Beijing, 100190, China

Abstract

Purpose: Development of more tumor-specific radiopharmaceuticals is not enough; to understand the disease, we must study data modeling. Although fluoro-18-deoxyglucose positron emission tomography can map a multi-peak distribution of trace radioisotopes, optical tomography should also be able to redirect the distribution.

Procedures: Multi-view image acquisition of small animals injected with 2-deoxy-2-[^{18}F]fluoro-D-glucose began with X-ray computed tomography scanning and Cerenkov luminescence imaging. After fusion processing, utilization of the geometric row scaling and $L_{1/2}$ regularization operator effectively generates *in vivo* Cerenkov luminescence tomography images with the SP_3 forward model.

Results: The identification is confirmed by the comparison between tumor-specific tomography from Cerenkov emission and the radioactivity measured *in vitro*.

Conclusion: The proposed technique can quickly localize the mobility of radionuclides and uptake by organs, which provides an imaging methodology in oncology.

Key words: Cerenkov radiation, Tomography, ^{18}FDG, Imaging radiopharmaceuticals

Introduction

The emergence of Cerenkov luminescence imaging (CLI) declares that positron emission tomography (PET) and single-photon emission computed tomography (SPECT) are no longer the only means of *in vivo* radionuclide imaging. This CLI technique has a solid physical basis that is due to Cerenkov emission from energetic α and β particles [1]. Estimate of the number of radiated Cerenkov photons can be obtained on the known classical and quantum Vavilov–Cerenkov radiation theory, which is already sufficient for the possibility of viewing. Measurement of the Vavilov–Cerenkov radiation thus provides a route for finding the distribution of medical isotopes. Tumor cells are highly glycolytic with increased expression of glycolytic enzymes and hexokinase activity. So 2-deoxy-2-[^{18}F]fluoro-D-glucose (^{18}FDG), used to assay cellular glucose uptake and utilization, is the most commonly employed and studied radiotracer in clinics after the approval of the Food and Drug Administration. Although ^{18}FDG is not a highly specific radiotracer for imaging malignant disease, mapping of ^{18}FDG uptake could provide a precursor to tumor-specific tomography imaging with the same methodology in future.

CLI is primarily qualitative [2–13], but its output is a planar image without depth information. Spinelli and colleagues used the diffusion approximation (DA) theory to estimate the light-source depth with multispectral data, which was based on the source-theoretic description of Cerenkov radiation for zero temperature in an isotropic homogeneous medium [14–16]. It was a painted two-dimensional image only by use of the planar light information from a fixed angle. However, it is important for biological and chemical progress to have physical position of the light source (0–360°) and its height (0–90°). In order to display the three-dimensional depth and refer to bioluminescence tomography reconstruction in the DA model,

Correspondence to: Jie Tian; *e-mail:* tian@ieee.org

optical tomography came true: Li firstly proposed the concept of Cerenkov luminescence tomography (CLT) with homogeneous optical properties [17]; almost at the same time as this, the reconstruction algorithm with optical property heterogeneity was studied by Zhong *et al.* after August 2009 [18].

The CLT problem includes both a forward model and an inverse reconstruction. As for a forward model in terms of accuracy, the higher-order spherical harmonics approximation could generate a more transport-like solution to the equation of radiation transport (ERT) than the DA method [19–21], especially for the Cerenkov continuum. The effectiveness of the CLT algorithm was confirmed, including the third-order simplified spherical harmonics (SP_3) approximation model and the elastic net regulation for CLT [22]. Based on our understanding of the research, there is a new but fatal problem in the application: reconstruction speed. Medical isotopes are ordinarily injected in organs at very low levels. This distribution may be dynamic and multi-modal, owing to metabolism and cell function. The fast reconstruction methodology gradually evolves into a real challenge for the scientific method.

Sparse reconstruction provides a strategy for rapid imaging. L_q regularization generates a sparse solution of ill-posed linear system with minimal L_q quasinorm. It is the sparest solution of the underdetermined linear system that is guaranteed *via* $L_{1/2}$ regularization [23, 24]. $L_{1/2}$ regularization theory has been applied to solve sparsity-promoting problems in compressed sensing. Here is the sparser solution, and there is the faster reconstruction of radiotracers' distribution. An inverse model inspired by the $L_{1/2}$ regularization theory is thus proposed for pharmacodynamic and pharmacokinetic imaging, coupled with a preconditioner of accelerating the iterative convergence.

The paper is organized as follows: A brief description of optical Cerenkov emission in radiative transfer theory and the reconstruction algorithm behind fast tumor-specific imaging are presented. In the "Results" section, attention is focused on the *in vivo* tomographic imaging of ^{18}FDG uptake using Cerenkov photons and *in vitro* measurements by directly detecting the beta particles themselves. Fast and efficient data modeling is presented for underdetermined reconstruction to identify the intrinsic variables. A discussion about features of the data modeling and some potential applications of the proposed Cerenkov luminescence tomography is presented. Finally, conclusions of this contribution follow.

Materials and Methods

Materials

^{18}FDG was provided by the Department of Nuclear Medicine, Beijing Union Medical College Hospital. Fenestra LC was purchased from Advanced Research Technologies Inc., Saint-Laurent, QC, Canada.

Cerenkov Emission in Radiative Transfer Theory

The optical Cerenkov radiance ϕ in the small animal Ω can be defined by an integrodifferential equation approximated from Maxwell's equations [25]:

$$\left\{\hat{s}\cdot\nabla + \mu_a + \mu_s + \frac{\partial}{\partial t}\right\}\phi(r,\ \hat{s},\ t) = q(r,\ \hat{s},\ t) + \mu_s \int p(\hat{s}',\ \hat{s})\phi(r,\ \hat{s}',\ t)\mathrm{d}\Omega' \qquad (1)$$

Radiance ϕ represents the spectral radiance integrated over a frequency range with units of watts per square millimeter per steradian, r is the spatial position, $\hat{s}$ indicates the unit direction vector, t denotes time, μ_a is the absorption coefficient, μ_s is the scattering coefficient, $\mathrm{d}\Omega$ denotes a differential solid angle element around direction $\hat{s}$, $\mathrm{d}\Omega'$ denotes a differential solid angle element around direction $\hat{s}'$, $p(\hat{s}',\ \hat{s})$ is the phase function, and the product $p(\hat{s}',\ \hat{s})\mathrm{d}\Omega$ represents the probability of light with propagation direction $\hat{s}'$ being scattered into $\mathrm{d}\Omega$ around direction $\hat{s}$. $q(r,\ \hat{s},\ t)\mathrm{d}v\mathrm{d}\Omega$ denotes the energy produced by a source in the volume element within the solid element per unit time.

It is useful to remember here that the SP_3 approximation to ERT yields a transport-like solution with the lowest computational cost, compared with equation solvers for biological tissues based on a higher-order spherical harmonics expansion. Utility of the finite element discretization generates a matrix equation derived from the SP_3 forward model [22],

$$J = GQ \qquad (2)$$

where J is the exiting partial current and source density $Q=(q_1, q_2, \ldots, q_N)^T$ in units of watts per square millimeter. $\mathbf{G}$ is an $M\times N$ formulated coefficient matrix.

Reconstruction Algorithm

The iterative method will lead to a solution for the ill-posed inverse problem. Considering that the stiffness matrix $\mathbf{G}$ derived from the nonlinear SP_3 approximation was formed by discontinuous coefficients. Before the iteration, geometric row scaling (GRS) is operated to require less iteration to achieve certain prescribed convergence criteria than the other preconditioners [26]. By $\mathbf{G_i}$ we denote the **i**-th row vector of nonsymmetrical $\mathbf{G}$, *i.e.*, $\mathbf{G_i}=(g_{i1},\ldots, g_{in})^T$. $\|\bullet\|_2^2$ is defined as the L_2 norm of a vector. If the **i**-th element of the diagonal matrix Λ is set to $\|G_i\|_2^2$, GRS is the operation of normalizing the equations:

$$\Lambda GQ = \Lambda J \qquad (3)$$

The non-invasively optical measurement C corresponding to J includes noises. So the computation for directly solving the inverse

linear equations may lead to a CLT reconstruction failure. In order to recover the distribution Q of radioisotopes, an optimization problem is defined as follows:

$$\min_{Q\in R^N}\left\{\|B-AQ\|_2^2+\lambda\|Q\|_{1/2}^{1/2}\right\} \tag{4}$$

where $\mathbf{A}=\Lambda\mathbf{G}$, $\mathbf{B}=\Lambda C$ which is an M-dimensional column vector, and the $L_{1/2}$ quasinorm of R^N is defined by $\|Q\|_{1/2}^{1/2}=\left(\sum_{i=1}^{N}|q_i|^{1/2}\right)^2$. λ is a positive regularization parameter. It is a non-convex and non-smooth optimization problem for mapping tumor-specific uptake of radiopharmaceuticals. The iterative half thresholding algorithm provides a fast approach for the solution in the large-scale optimization system, of which the operator shall be calculated in accordance with the following formula:

$$Q_{k+1}=P_{\lambda\xi}F_k=P_{\lambda\xi}\left(Q_k+\xi\mathrm{A}^T(\mathrm{B}-\mathrm{A}Q_k)\right) \tag{5}$$

and

$$\begin{cases}\lambda_k=4\|A\|_2^2(F_k)^{3/2}/(3N)\\ P_{\lambda\xi}=\left(p_{\lambda\xi}(q_1),\cdots,p_{\lambda\xi}(q_N)\right)^T\end{cases} \tag{6}$$

which is the k-th iterative solution. $p\lambda\xi(q)$ is defined by [25]

$$p_{\lambda\xi}(q)=\begin{cases}\frac{2}{3}q\left(1+\cos\left(\frac{2\pi}{3}-\frac{2\varphi_\lambda}{3}\right)\right), & |q|>\eta(\lambda\xi)^{\frac{2}{3}}\\ 0 & otherwise\end{cases} \tag{7}$$

In the paper, ξ was set to a constant value of $\left(1-10^{-10}\right)/\|A\|_2^2$, and $\varphi_\lambda(q_i)=\arccos\left(\lambda(|q_i|/3)^{-3/2}/8\right)$. The parameter η is a non-negative constant, which can be adjusted for CLT reconstruction. The number of iterations can be set in advance using empirical data or be determined dynamically depending on $\|Q_{k+1}-Q_k\|_2^2/\|Q_k\|_2^2$. In addition, the software framework for CLT was coded in C++, and the sparse computing and storage technology was explored in the calculation. When the variable is 0, it is discarded in the traversal process.

Digimouse

The test data are a digimouse [22] in numerical simulation. This data set was discretized into a tetrahedral mesh (4,245 points, 26,859 edges, 44,085 triangles, and 214,740 tetrahedrons) for CLT

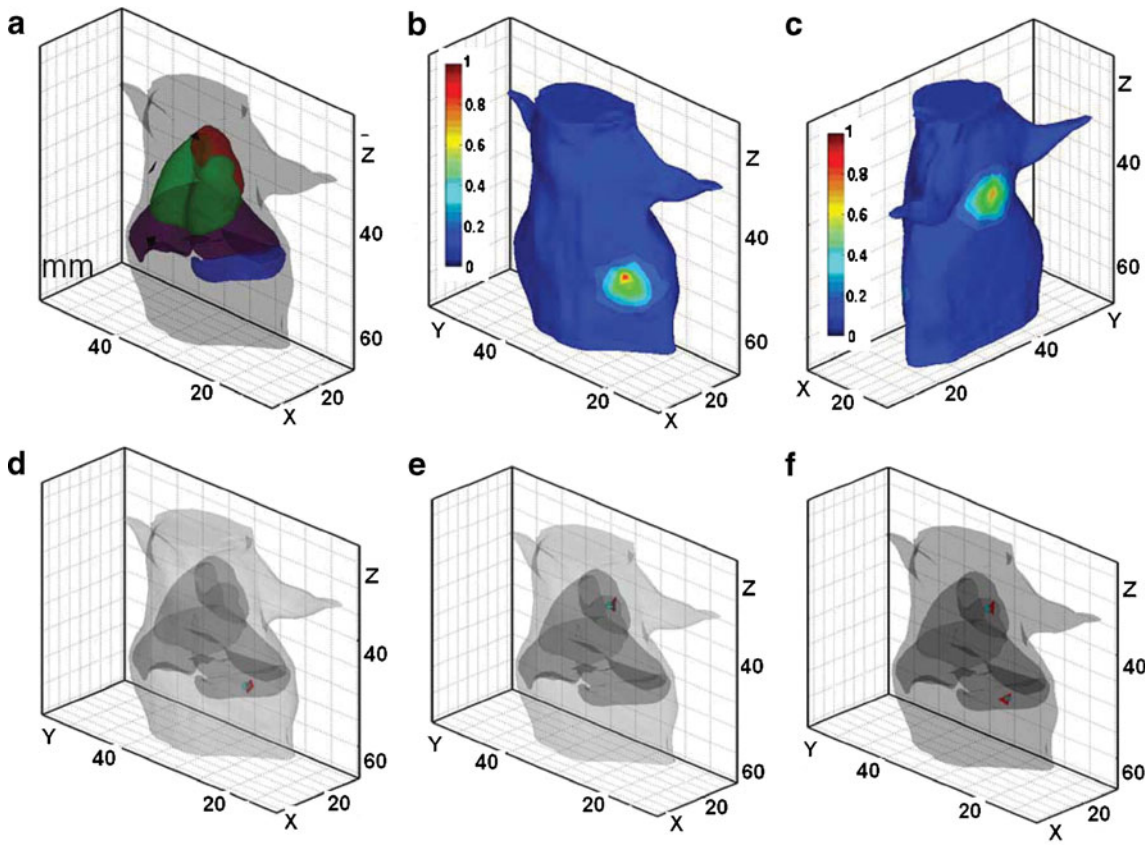

Fig. 1. Numerical experiments for CLT reconstruction. **a** The tetrahedral mesh; **b**, **c** the measured data from different perspectives by MC simulations in case 3, and the peak value of the flux densities is normalized to 1; **d**–**f** the experimental results.

reconstruction as shown in Fig. 1a. Simulated measurement data of the photon density along the digimouse surface were used for the source reconstruction. In order to fully verify the robustness of the algorithm, three cases were designed as follows: case 1, assuming a point light source (17.0, 31.6, and 38.4 mm) is located within the heart; case 2, assuming a point light source (21.3, 23.6, and 50.8 mm) is inside the stomach; and case 3, assuming the above two-point light sources in the body occur at the same time. The number of photons was set to 10^6 for each one light source with the shortest distance being 3 mm from the surface. Fig. 1b, c shows the simulated measurement data in case 3. The weighted optical parameters of the digimouse are shown in Table 1, so as to model the mixed optical spectrum in the physical experiment. μ_s' stands for the reduced optical scattering coefficient in the paper.

Animal Model

22B-cell tumor-bearing BALB/c nude mice were kindly provided by the Medical Isotopes Research Center, Peking University. Animal experimentation was conducted under approved research protocols of the Animal Care and Use Committee.

In Vivo Multimodality Imaging

A 20.7-g tumor-bearing mouse was anesthetized with 2.0% isoflurane delivered in medical air; 0.2 mL of Fenestra LC and 0.1 mL of ^{18}FDG were injected *via* its tail vein. The *in vivo* radioactivity of the mouse was measured at 60 min after injection by a RM-905a type standard Grade Radioactivity Meter (Beijing Puxiang Technology Co., Ltd. Beijing, People's Republic of China), of which the value was 14,541 kBq. Anesthesia was again induced with an intraperitoneal injection of 1 g/kg urethane (0.2 mL, in saline), in order to quell the movement of the chest before CT imaging. The anesthetized mouse was then scanned by X-ray micro-CT at a voltage of 50 kVp and an exposure time of 0.47 s for 12 min. The optical imaging system was activated after obtaining structural information. Four planar Cerenkov luminescence images were acquired in a dark room with the aperture number *f* to 2.8, the binning value equal to 2, and the exposure time equal to 120 s. Finally, four corresponding photograph images of the mouse were collected with the binning value equal to 1 and the exposure time equal to 30 ms. Fig. 2 is the schematic diagram of optical detection. The work temperature of the back-illuminated CCD chip was −110 C through a liquid-nitrogen-cooled option for long exposures (Princeton Instruments VersArray 1300B, Roper Scientific, Trenton, NJ, USA). With 20×20 μm pixels, a quantum efficiency of well over 90% at 500–650 nm, 2 e^- CCD read noise, 3 e^- system read noise, 300 ke^- single-pixel full well, 250 ke^- output amplifier, 0.5 e^-/p/h dark current, and

Table 1. Optical parameters of the nude mouse [27], 10^{-2} mm^{-1}

Material	Muscle	Heart	Liver	Lungs	Stomach
$\mu_a(r)$	3.2	2.2	12.8	7.1	3.5
$\mu_s'(r)$	58.6	112.9	64.6	230.5	148.0

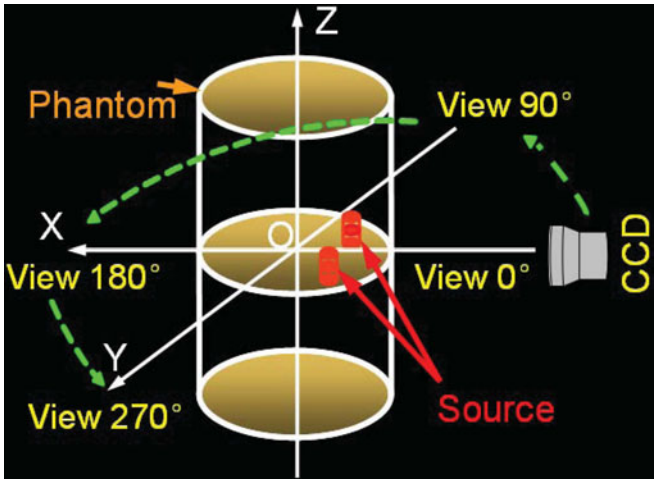

Fig. 2. Schematic diagram of Cerenkov optical detection.

100 kHz scan rates, this system provides a high spatial resolution imaging at very high sensitivity. *In vivo* imaging system control and image processing were performed on a personal computer with Intel(R) Core(TM) i5 CPU 650 at 3.2 GHz and 3 GB RAM.

Micro-CT and optical images are shown in Fig. 3a, b. The partial micro-CT data were segmented into tumors, muscle, heart, liver, lungs, stomach, bone, and kidneys (Fig. 3c). Optical measurements **B** on the mesh with 4,131 nodes, 45,000 triangles, and 22,138 tetrahedrons were used for CLT reconstruction (Fig. 3d). The weighted optical parameters of the mouse were used as optical property priors. In addition to the data in Table 1, μ_a(bone)=0.2 and μ_s'(bone)=93.5; μ_a(kidneys)=1.0 and μ_s'(kidneys)=83.0; these parametric values have units of 10^{-2} mm^{-1}.

Results

Numerical Reconstruction

Fig. 1d–f displays blue spheres with a diameter of 1 mm that locates the actual light source in cases 1, 2, and 3, respectively. The red tetrahedron element denotes the smallest discrete unit with the maximal value of light intensity distribution after CLT reconstruction. The actual point light sources were located at the spherical centers. Case 1: η was set to 160; the number of non-zero solutions to the CLT problem was 6, and the center of the red tetrahedron was 16.9, 31.0, and 38.0 mm with a distance error of 0.7 mm from the actual source. Case 2: η=180; there was only one non-zero solution; the tetrahedral center was 21.0, 23.2, and 50.6 mm with a distance error of 0.5 mm. Case 3: η=150; the number of non-zero solutions is four; tetrahedral centers were 16.6, 31.2, and 38.1 and 21.5, 23.3, and 50.8 mm with their distance errors of 0.6 and 0.4 mm. Every elapsed time for the whole-body reconstruction was about 0.8 s (M=1,147, N=21,470) in these cases.

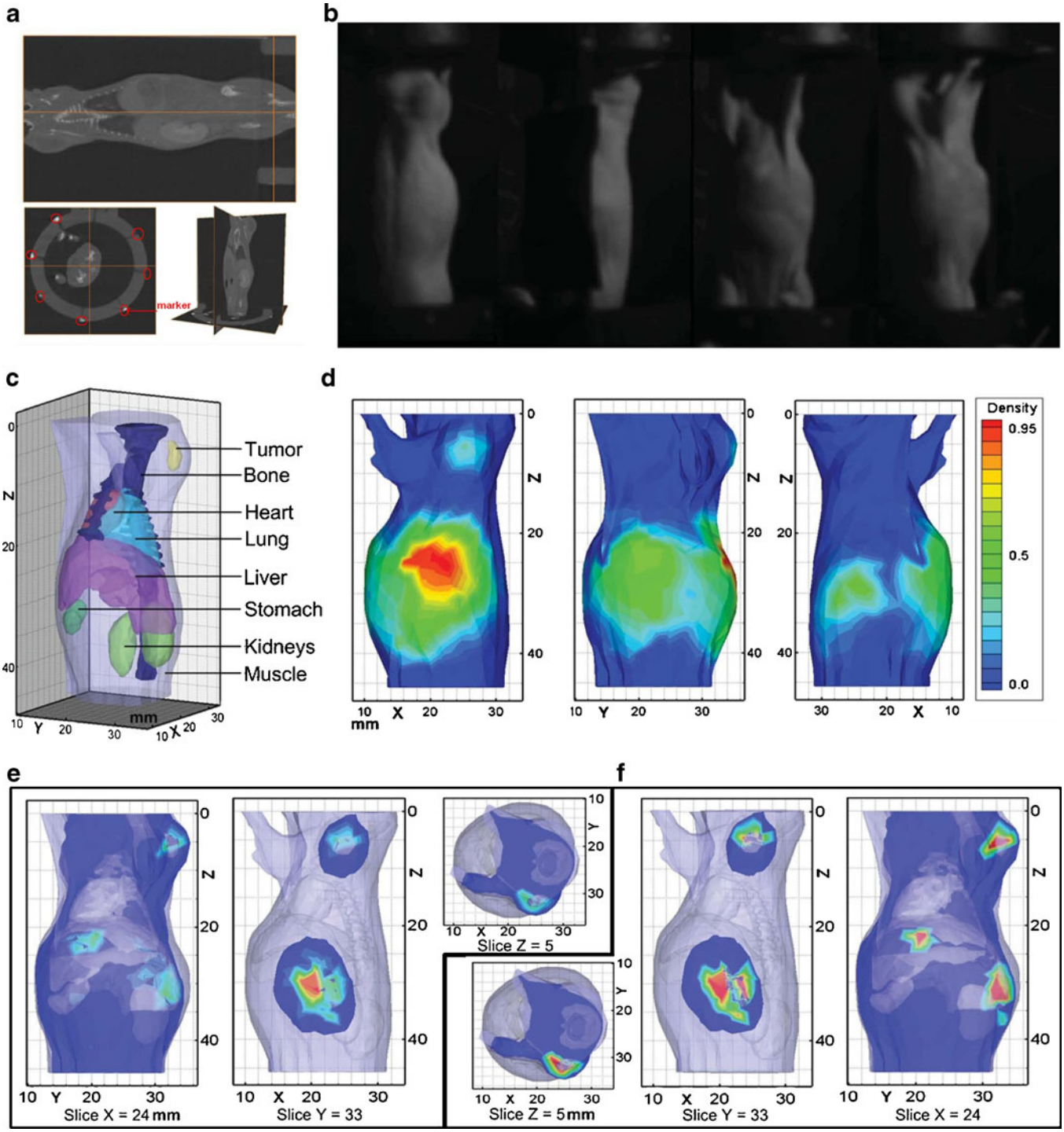

Fig. 3. Physical experiments for CLT reconstruction. **a** Micro-CT image and *red rings* denote the registration markers between micro-CT and Cerenkov luminescence imaging; **b** optical images; **c** a segmented mouse; **d** the normalized Cerenkov luminescence distribution without outliers, of which the peak value is 13.6 nW mm^{-2}; **e**, **f** slices of CLT using elastic net penalty and the proposed algorithm, respectively, where the *red region* is located at the element with the largest energy intensity.

In Vivo Application

Fig. 3f shows three slices from reconstructed results through the center point (24, 33, and 5 mm) for tumor cells. The elapsed time for the whole-body CLT reconstruction was 0.5 s (η=115, M=726, N=22,138). In order to demonstrate the proposed algorithm, we also performed CLT reconstruction with elastic net regularization *via* a coordinate descent, where program parameter settings were illustrated in the literature [22]. Although the resulted location was also accurate, the elapsed time for this CLT reconstruction was 16,490.7 s.

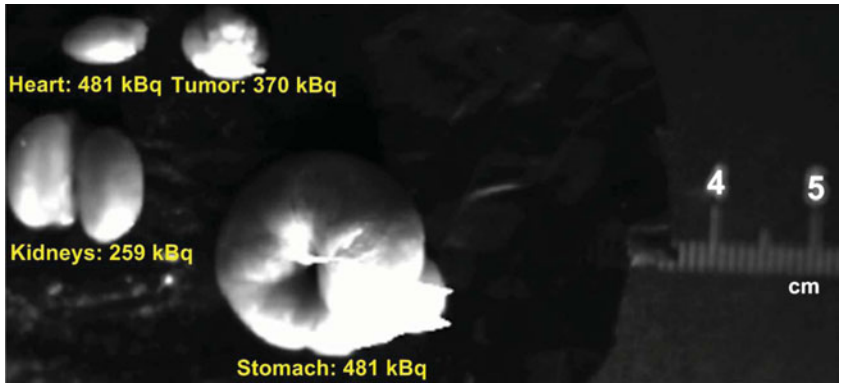

Fig. 4. Schema of *in vitro* specific radioactivity in separate tissues.

In Vitro Measurements

The *in vitro* measurements were completed by directly detecting the beta radioactivity with the RM-905a type standard Grade Radioactivity Meter after *in vivo* imaging. The radioactivity in the whole mouse amounted to 12,210 kBq. The specific radioactivity in a separate tissue was measured, *i.e.*, tumor, 370 kBq; heart, 481 kBq; kidneys, 259 kBq; and stomach, 481 kBq (Fig. 4). The tumor volume was approximately equal to 64 mm^3 in accordance with grid coordinates, which had a maximum diameter of 8 mm. The *ex vivo* data were consistent with the experimental results in that the reconstructed intensity in the region of the stomach was larger than that in the tumor.

Discussion

Several striking features of real data sets are the actual challenges for the application of the CLT technique. The dimension ratio (N/M) between the unknown S and known $\mathbf{B}$ is 18.7 in numerical experiments or 30.5 in physical experiments. The coefficient matrix $\mathbf{A}$ of the three-dimensional whole-body reconstruction has a high dimension. The $L_{1/2}$ regulation theory yields a consistent data model, when jointed with the sparse computing and storage technology. The percent of non-zero elements in the total unknown variables was less than 2.0%, and the whole-body reconstruction time of CLT was less than 0.8 s in simulation and *in vivo* experiments, which was associated with no more than a 0.7-mm location error. In a word, although limitation of the optical blurring effect and low levels of the transmitted light may restrict the application of CLT in some fields in clinics, the proposed method provides a fast and effective multi-peak reconstruction strategy fusing the complementary advantages of X-ray CT, optical and nuclear imaging with the same biomarker [28, 29].

There are several potential applications of the proposed data model for solving biological problems including: (1) It enables multifunctional data acquisitions and near-contemporaneous fusion of structural and metabolic data within short periods of time including the use of medical isotopes with very short half-lives [30]. (2) The existence of multidrug tolerant organisms promotes the development of multi-target drugs. Functionally significant epigenetic alterations seem to be factors not only in cancer cells but also in altered cells of the tumor-associated stroma [31]. Reconstruction of multi-biomarkers and multi-peak distribution at the same time becomes essential, which will be solved by the proposed method. (3) The technique provides a potential clinical application for early diagnosis and treatment of cancers, such as eye or prostate tumors when the suitable dark room is designed for humans. (4) CLT is a low-cost measurement, when the complexity and infrastructure needs of PET/SPECT limit their accessibility and effect for early detection [32].

Conclusion

The methodology of Cerenkov luminescence tomography with geometric row scaling and $L_{1/2}$ regulation provides a fast low-cost nuclear medical imaging. The *in vivo* experimental results also indicate that this emerging field is taking increasingly progressive steps toward the clinical application. The proposed technology is important not only for detecting disease but also for characterizing and assessing change of the disease with time or therapy.

Acknowledgments. This paper is supported by the National Basic Research Program of China (973 Program) under grant no. 2011CB707700; the Knowledge Innovation Project of the Chinese Academy of Sciences under grant no. KGCX2-YW-907; the National Natural Science Foundation of China under grant nos. 81027002, 81071205, and 30970778; the Fellowship for Young International Scientists of the Chinese Academy of Sciences under grant no. 2010Y2GA03; and the Chinese Academy of Sciences Visiting Professorship for Senior International Scientists under grant no. 2010T2G36.

Conflict of Interest Statement. None.

References

1. Cerenkov PA (1934) Visible luminescence of pure liquids under action of γ-radiation. Doklady Akad Nauk (USSR) 2:451–454
2. Burch WM (1971) Cerenkov light from ^{32}P as an aid to diagnosis of eye tumours. Nature 234:358
3. Robertson R, Germannos MS, Li C, Mitchell GS, Cherry SR, Silva MD (2009) Optical imaging of Cerenkov light generation from positron-emitting radiotracers. Phys Med Biol 54:N355–N365
4. Cho JS, Taschereau R, Olma S et al (2009) Cerenkov radiation imaging as a method for quantitative measurements of beta particles in a microfluidic chip. Phys Med Biol 54:6757–6771
5. Liu H, Ren G, Miao Z et al (2010) Molecular optical imaging with radioactive probes. PLoS One 5:e9470
6. Dothager RS, Goiffon RJ, Jackson E, Harpstrite S, Piwnica-Worms D (2010) Cerenkov radiation energy transfer (CRET) imaging: a novel method for optical imaging of PET isotopes in biological systems. PLoS One 5:e13300
7. Lewis MA, Kodibagkar VD, ÄOz OK, Mason RP (2010) On the potential for molecular imaging with Cerenkov luminescence. Opt Lett 35:3889–3891
8. Liu H, Zhang X, Xing B, Han P, Gambhir SS, Cheng Z (2010) Radiation-luminescence-excited quantum dots for *in vivo* multiplexed optical imaging. Small 6:1087–1091
9. Liu H, Ren G, Liu S et al (2010) Optical imaging of reporter gene expression using a positron-emission-tomography probe. J Biomed Opt 15:060505
10. Ruggiero A, Holland JP, Lewis JS, Grimm J (2010) Cerenkov luminescence imaging of medical isotopes. J Nucl Med 51:1123–1130
11. Park JC, An GI, Park S et al (2011) Luminescence imaging using radionuclides: a potential application in molecular imaging. Nucl Med Biol 38:321–329
12. Lucignani G (2011) Cerenkov radioactive optical imaging: a promising new strategy. Eur J Nucl Med Mol Imaging 38:592–595
13. Ran C, Zhang Z, Hooker J, Moore A (2011) *In vivo* photoactivation without light: use of Cherenkov radiation to overcome the penetration limit of light. Mol Imaging Biol. doi:10.1007/s11307-011-0489-z
14. Jelley JV (1955) Cerenkov radiation and its applications. Br J Appl Phys. doi:10.1088/0508-3443/6/7/301
15. Spinelli AE, D'Ambrosio D, Calderan L, Marengo M, Sbarbati A, Boschi F (2010) Cerenkov radiation allows *in vivo* optical imaging of positron emitting radiotracers. Phys Med Biol 55:483–495
16. Boschi F, Calderan L, D'Ambrosio D et al (2011) *In vivo*^{18}F-FDG tumour uptake measurements in small animals using Cerenkov radiation. Eur J Nucl Med Mol Imaging 38:120–127
17. Li C, Mitchell GS, Cherry SR (2010) Cerenkov luminescence tomography for small animal imaging. Opt Lett 35:1109–1111
18. Zhong J, Qin C, Yang X, Zhu S, Zhang X, Tian J (2011) Cerenkov luminescence tomography for *in vivo* radiopharmaceutical imaging. Int J Biomed Imaging 2011:641618
19. Lu Y, Machado HB, Bao Q et al (2010) *In vivo* mouse bioluminescence tomography with radionuclide-based imaging validation. Mol Imaging Biol 13:53–58
20. Liu K, Lu Y, Tian J et al (2010) Evaluation of the simplified spherical harmonics approximation in bioluminescence tomography through heterogeneous mouse models. Opt Express 18:20988–21002
21. Klose AD (2010) The forward and inverse problem in tissue optics based on the radiative transfer equation: a brief review. J Quant Spectrosc Ra 11:1852–1853
22. Zhong J, Tian J, Yang X, Qin C (2011) Whole-body Cerenkov luminescence tomography with the finite element SP_3 method. Ann Biomed Eng 39:1728–1735
23. Foucart S, Lai M (2009) Sparsest solutions of underdetermined linear systems via lq-minimization for $0<q\leq 1$. Appl Comput Harmon Anal 26:395–407
24. Xu Z (2010) Data modeling: visual psychology approach and $L_{1/2}$ regularization theory. In: Proceedings of the International Congress of Mathematicians, Section 18, Hyderabad, India
25. Arridge SR, Schotland JC (2009) Optical tomography: forward and inverse problems. Inverse Probl 25:123010
26. Gordon D, Gordon R (2010) CARP-CG: a robust and efficient parallel solver for linear systems, applied to strongly convection dominated PDEs. Parallel Comput 36:495–515
27. Alexandrakis G, Rannou FR, Chatziioannou AF (2005) Tomographic bioluminescence imaging by use of a combined optical (OPET) system: a computer simulation feasibility. Phys Med Biol 50:4225–4241
28. Tian J, Bai J, Yan X et al (2008) Multimodality molecular imaging. IEEE Eng Med Biol 27:48–57
29. Poste G (2011) Bring on the biomarkers. Nature 469:156–157
30. Yu E, Muzi M, Hackenbracht JA et al (2011) C11-acetate and F-18 FDG PET for men with prostate cancer bone metastases: relative findings and response to therapy. Clin Nucl Med 36:192–198
31. Hanahan D, Weinberg RA (2011) Hallmarks of cancer: the next generation. Cell 144:646–674
32. Moses H III, Martin JB (2011) Biomedical research and health advances. N Engl J Med 364:567–571